ELSEVIER

International Journal of Heat and Fluid Flow 22 (2001) 381–392

International Journal of HEAT AND FLUID FLOW

www.elsevier.com/locate/ijhff

Predicting turbulent convective heat transfer in fully developed duct flows

Masoud Rokni [a,*], Thomas B. Gatski [b]

[a] *Division of Heat Transfer, Lund Institute of Technology, P.O. Box 118, 221 00 Lund, Sweden*
[b] *Computational Modeling and Simulation Branch, NASA Langley Research Center, Hampton, VA 23681-2199, USA*

Received 8 December 1999; accepted 27 January 2001

Abstract

The performance of an explicit algebraic stress model (EASM) is assessed in predicting the turbulent flow and forced heat transfer in both straight and wavy ducts, with rectangular, trapezoidal and triangular cross-sections, under fully developed conditions. A comparison of secondary flow patterns, including velocity vectors and velocity and temperature contours, are shown in order to study the effect of waviness on flow dynamics, and comparisons between the hydraulic parameters, Fanning friction factor and Nusselt number, are also presented. In all cases, isothermal conditions are imposed on the duct walls, and the turbulent heat fluxes are modeled using gradient-diffusion type models. The formulation is valid for Reynolds numbers up to 10^5 and this minimizes the need for wall functions that have been used with mixed success in previous studies of complex duct flows. In addition, the present formulation imposes minimal demand on the number of grid points without any convergence or stability problems. Criteria in terms of heat transfer and friction factor needed to choose the optimal wavy duct cross-section for industrial applications among the ones considered are discussed.

1. Introduction

The performance of turbulence and heat transfer models in predicting the velocity and temperature fields of relevant industrial flows has become increasingly important during the last few years. This requirement for improved predictive performance is also true for turbulent duct flows which occur frequently in many industrial applications, such as compact heat exchangers, gas turbine cooling systems, recuperates, cooling channels in combustion chambers, inter-coolers, nuclear reactors, and others. The cross-section of these ducts might be both orthogonal (square or rectangular) and non-orthogonal (such as trapezoidal), in which the generated flow is extremely complex. Sometimes, the ducts are also wavy or corrugated in the streamwise direction and might be manufactured with ribs in order to achieve faster transition to turbulence.

Several fundamental studies of turbulent flow in square and rectangular ducts exist in the literature. Direct numerical simulations have been carried out for a square duct by Gavrilakis (1992) and Huser and Biringen (1993) with Reynolds numbers of 4410 and 10^4, respectively. Large eddy simulations of square and rectangular ducts have been reported by Madabhushi and Vanka (1991) at a Reynolds number of 5800, and by Su and Friedrich (1994) and Meyer and Rehme (1994) at Reynolds numbers up to 4.9×10^4. Nevertheless, limitations on computational power and memory make it almost impossible to directly solve for the turbulent flow field in practical engineering duct flows using a direct numerical simulation for the foreseeable future. Large eddy simulations may be more tractable; although to date, their use has not been widespread. Thus, the prediction of the turbulent flow and heat transfer characteristics in engineering duct flows still requires a Reynolds-averaged approach using suitable turbulent closure models for both the velocity and temperature correlations.

It is known that secondary motions develop in the corners of non-circular straight ducts in the plane perpendicular to the streamwise flow direction. These motions are turbulence-induced and are commonly referred to as motions of Prandtl's *second* kind. Such motions are of importance since they redistribute the kinetic energy, influence the streamwise velocity, and thereby affect the wall shear stress and heat transfer. The effect of secondary motions of Prandtl's second kind on the wall shear stresses and heat fluxes increases considerably when the ducts are corrugated. Even though linear eddy viscosity models are one of the most popular models among engineers – owing to their simplicity and overall good performance properties – they do not have the ability to predict such secondary flows. Previously, Rokni and Sundén (1996, 1998) employed a non-linear eddy viscosity model, coupled with wall functions, to predict the flow field and heat fluxes in a straight and wavy duct with trapezoidal cross-sections. This level of closure accounted for the Reynolds stress anisotropy and could, therefore, be used to predict these secondary flow fields.

* Corresponding author. Tel.: +46-2228604; fax: +46-2228612.
E-mail address: masoud.rokni@vok.lth.se (M. Rokni).

0142-727X/01/$ - see front matter
PII: S0142-727X(01)00104-7

Another advantage of this level of closure is that such calculations can be achieved within the relative cost of a two-equation formulation.

No fundamental studies of turbulent flow in wavy ducts with triangular cross-section exist in the literature. As it is well known wall functions, which had been used previously (Rokni and Sundén, 1996, 1998), are not a general tool for predicting the recirculating zone in wavy ducts. Rokni (2000) successfully tested the stability of an explicit algebraic stress model (EASM) with damping functions in the Reynolds stress representations in a wavy duct; however, the detailed dynamics of the flow were not analyzed. That study focused on developing a very stable low-Reynolds version of an EASM and its implementation in a general CFD code. In the study reported here, the earlier work of Rokni and Sundén (1996, 1998) is extended to arbitrary ducts using an EASM suitable for both low- and high-Reynolds numbers. Damping functions are only used in the turbulent diffusion models needed in both the turbulent kinetic energy and dissipation rate equations. The method is applied to straight and wavy ducts with rectangular, trapezoidal, and triangular cross-sections. A comparison of secondary flow patterns between the straight and wavy ducts with similar cross-section and aspect ratio are used to analyze the effect of waviness on flow dynamics. Isothermal wall conditions are assumed for all the configurations studied, and the turbulent heat flux model used is a generalized gradient-diffusion hypothesis model (GGDH). Although this model has been used previously in related duct flow studies, the current formulation introduces bounds on the turbulent time-scale delimited by the Kolmogorov and mean flow time scales.

2. Mean flow and turbulent equations

A Reynolds-averaged Navier–Stokes (RANS) approach is used to predict the fully developed turbulent flow and heat transfer in the various ducts. The governing equations for the mean velocity and temperature are

$$\frac{\partial U_j}{\partial x_j} = 0, \tag{1}$$

$$\frac{\partial U_i}{\partial t} + \frac{\partial}{\partial x_j}\left(U_i U_j\right) = -\frac{1}{\rho}\frac{\partial P}{\partial x_i} + \frac{\partial}{\partial x_j}\left[\nu \frac{\partial U_i}{\partial x_j}\right] - \frac{\partial}{\partial x_j}\left(\overline{u_i u_j}\right), \tag{2}$$

$$\frac{\partial T}{\partial t} + \frac{\partial}{\partial x_j}\left(U_j T\right) = \frac{\partial}{\partial x_j}\left[\frac{\nu}{Pr}\frac{\partial T}{\partial x_j}\right] - \frac{\partial}{\partial x_j}\left(\overline{u_j t}\right), \tag{3}$$

where the turbulent stresses $\overline{u_i u_j}$ and turbulent heat fluxes $\overline{u_j t}$ require modeling in order to close the equations. An EASM will be used for the turbulent stresses and the turbulent heat fluxes will be modeled using three different gradient-diffusion models.

2.1. Explicit algebraic stress model

Algebraic stress models originate from Reynolds stress closures under assumptions about the convective and diffusive terms (e.g., Gatski and Speziale, 1993). The resulting implicit algebraic equation for the Reynolds stress anisotropy b_{ij} is

$$-\frac{1}{a_4}b_{ij} - a_3\left(b_{ik}S_{kj} + S_{ik}b_{kj} - \frac{2}{3}b_{mn}S_{nm}\delta_{ij}\right) + a_2\left(b_{ik}W_{kj} - W_{ik}b_{kj}\right) = R_{ij}, \tag{4}$$

where the stress anisotropy b_{ij}, mean strain rate S_{ij}, and mean rotation rate tensors W_{ij} are given, respectively, by

$$b_{ij} = \frac{\overline{u_i u_j}}{2k} - \frac{1}{3}\delta_{ij}, \quad S_{ij} = \frac{1}{2}\left(\frac{\partial U_i}{\partial x_j} + \frac{\partial U_j}{\partial x_i}\right), \quad W_{ij} = \frac{1}{2}\left(\frac{\partial U_i}{\partial x_j} - \frac{\partial U_j}{\partial x_i}\right) \tag{5}$$

and the coefficients a_i are directly related to the pressure–strain correlation model used to close the Reynolds stress transport equation. In this study, the linearized form of the SSG pressure–strain model is used (see Speziale et al., 1991; Gatski and Speziale, 1993).

Since Eq. (4) represents an implicit set, the numerical robustness of its solution can be questionable. The EASM used here replaces this implicit relation with a polynomial expansion in a tensor basis. In two-dimensional flows, the three-term basis used here is exact, while in three-dimensional flows it is taken as a low-order approximation to the full ten-term basis. In addition, an isotropic dissipation rate is assumed so that $R_{ij} = a_1 S_{ij}$. The explicit algebraic model used here is an extension of the Gatski and Speziale (1993) model and is described in Rumsey et al. (2000).

The resulting explicit expression is:

$$b_{ij} = \alpha_1 S_{ij} + \alpha_2\left(S_{ik}W_{kj} + S_{jk}W_{ki}\right) + \alpha_3\left(S_{ik}S_{kj} - \frac{1}{3}S_{mn}S_{mn}\delta_{ij}\right), \tag{6}$$

where the α_i's are scalar coefficient functions of the invariants

$$\eta^2 = S_{ij}S_{ij}, \quad \xi^2 = W_{ij}W_{ij} \tag{7}$$

and are given by

$$\alpha_1^3 - \frac{\gamma_1}{\gamma_0\eta^2\tau}\alpha_1^2 + \frac{1}{4\gamma_0^2\eta^4\tau^2}\left[\gamma_1^2 - 2\tau^2\gamma_0 a_1\eta^2 - 2\eta^2\tau^2\left(\frac{a_3^2}{3} - \Re^2 a_2^2\right)\right]\alpha_1 + \frac{\gamma_1 a_1}{4\gamma_0^2\eta^4\tau} = 0, \tag{8}$$

$$\alpha_2 = a_2 a_4 \alpha_1 \quad \text{and} \quad \alpha_3 = -2a_3 a_4 \alpha_1 \tag{9}$$

with

$$a_1 = 0.487, \quad a_2 = 0.80, \quad a_3 = 0.375, \quad a_4 = g\tau, \quad \tau = k/\varepsilon, \tag{10}$$

$$g = \left(\gamma_1 - 2\gamma_0\alpha_1\eta^2\tau\right)^{-1}, \quad \gamma_0 = 1.9, \quad \gamma_1 = 0.7, \quad \Re^2 = \frac{\xi^2}{\eta^2}. \tag{11}$$

The proper choice for α_1 is the minimum real root of Eq. (8) (Jongen and Gatski, 1999).

The EASM formulation used requires the solution of transport equations for the turbulent kinetic energy k and the turbulent dissipation rate ε which are given in the form

$$\frac{\partial k}{\partial t} + \frac{\partial}{\partial x_j}\left(U_j k\right) = \frac{\partial}{\partial x_j}\left[\left(\nu + \frac{\nu_t}{\sigma_k}\right)\frac{\partial k}{\partial x_j}\right] - \overline{u_i u_j}\frac{\partial U_i}{\partial x_j} - \varepsilon, \tag{12}$$

$$\frac{\partial \varepsilon}{\partial t} + \frac{\partial}{\partial x_j}\left(U_j \varepsilon\right) = \frac{\partial}{\partial x_j}\left[\left(\nu + \frac{\nu_t}{\sigma_\varepsilon}\right)\frac{\partial \varepsilon}{\partial x_j}\right] - C_{\varepsilon 1}\frac{\varepsilon}{k}\overline{u_i u_j}\frac{\partial U_i}{\partial x_j} - f_\varepsilon C_{\varepsilon 2}\frac{\varepsilon^2}{k}. \tag{13}$$

The constants $C_{\varepsilon 1}$ and $C_{\varepsilon 2}$ are set to 1.44 and 1.83, respectively and the turbulent eddy viscosity ν_t is calculated as

$$\nu_t = f_\mu C_\mu \frac{k^2}{\varepsilon}, \tag{14}$$

where $C_\mu = 0.09$. The damping function f_μ only appears in the isotropic eddy viscosity that is used in the model for the turbulent transport in both the kinetic energy and dissipation rate equations, and the function f_ε is required to avoid any singularities in the destruction-of-dissipation term as the wall is approached. Both f_ε and f_μ asymptote to unity in the fully turbulent region remote from the solid walls. In this study, the Abe et al. (1995) forms for f_ε and f_μ are used

$$f_\varepsilon = \left(1 - \mathrm{e}^{-(y^*/3.9)}\right)^2 \left(1 + 0.19\mathrm{e}^{-(Re_\tau/3.5)^2}\right),$$
$$f_\mu = \left(1 - \mathrm{e}^{-(y^*/16)}\right)^2 \left(1 + \frac{4}{Re_\tau^{0.75}}\mathrm{e}^{-(Re_\tau/200)^2}\right), \tag{15}$$

where

$$y^* = u_\varepsilon \frac{d}{\nu} = (\nu\varepsilon)^{0.25}\frac{d}{\nu}, \quad Re_\tau = \frac{k^2}{\nu\varepsilon} \tag{16}$$

and d is the normal distance to the nearest wall. Both σ_k and σ_ε are set to 1.4 (Abe et al., 1995). The original set of coefficients used in Eqs. (15) and (16) were calibrated with $C_{\varepsilon 1} = 1.5$ and $C_{\varepsilon 2} = 1.9$ (Abe et al., 1995). In this study, $C_{\varepsilon 1} = 1.44$ and $C_{\varepsilon 2} = 1.83$ are used and, therefore, the coefficients used in Eqs. (15) and (16) have been recalibrated against DNS channel flow data (Kim et al., 1987).

Fig. 1 shows the calibration results for the present model in comparison with the DNS data of Kim et al. (1987). A linear eddy viscosity model (original Abe et al., 1995) using damping function (f_μ) in the Reynolds stresses and turbulent viscosity has also been included for comparison. As can be seen both models match the mean velocity and turbulent shear stress data very well. For the turbulent kinetic energy, both models match the DNS data beyond about y^+ of 50. The EASM does not match the peak values since the damping function f_μ is not used in the EASM constitutive relation, Eq. (6). As noted previously for the EASM, the eddy viscosity ν_t, which appears in the diffusion terms of the kinetic energy and dissipation rate equations, is the only place where f_μ enters. The procedure ensures that the log–law is correct and consequently that the wall skin-friction is correct. The result of this, however, is that the peak in the normal stresses will be under-predicted. While the LEVM predicts the turbulent kinetic energy rather well, the individual components are less consistent due to the isotropic structure of the eddy viscosity.

2.2. Turbulent heat flux model

Previous studies by Rokni and Sundén (1998) and Rokni (2000) have assessed different heat flux models. These have included a simple eddy diffusivity mode, a model based on a GGDH, and a model based on the WET method (Launder, 1988). Both the GGDH model and the WET model outperformed the simple eddy diffusivity model.

For the study here, the GGDH model is used; however, it is modified relative to the previous studies by accounting for the time-scale variation in the near-wall region. The GGDH based model is dependent on the mean temperature gradient and is given by

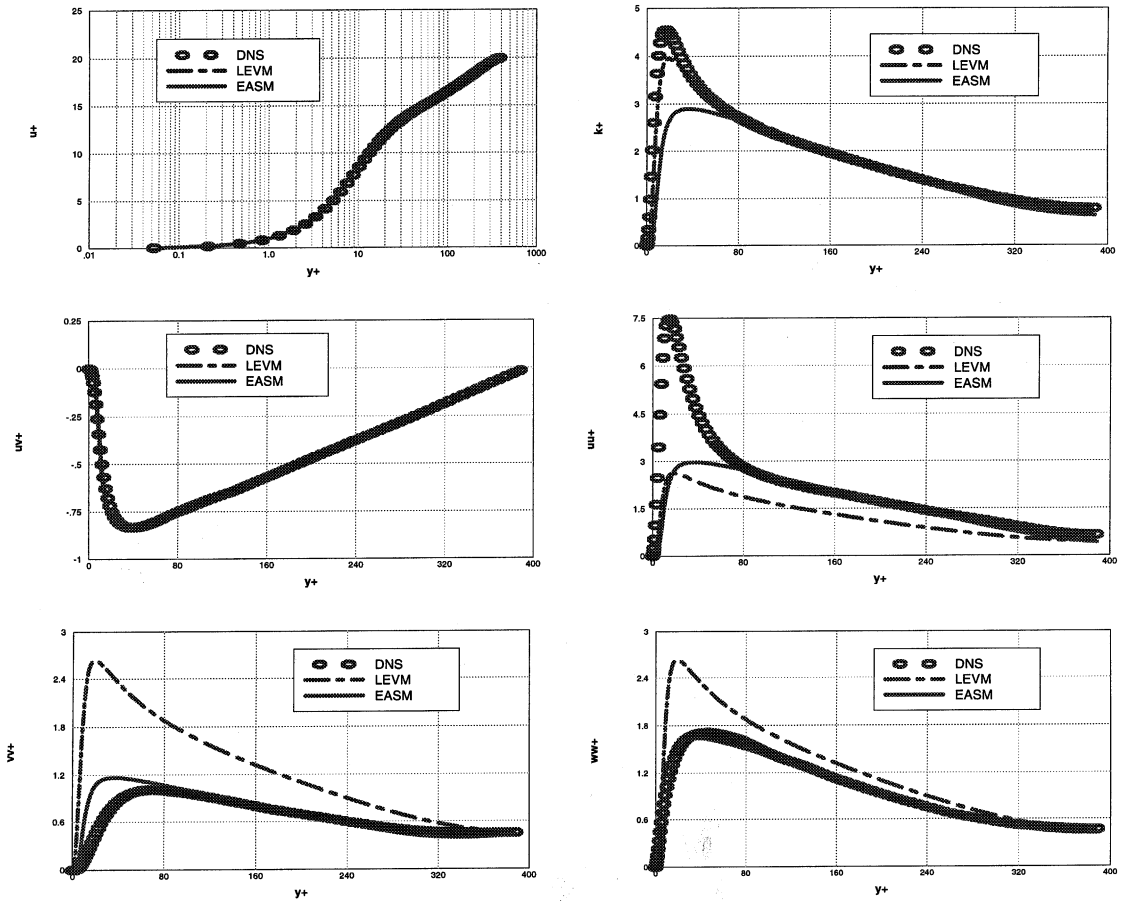

Fig. 1. Comparison between the DNS data (Kim et al., 1987) and present model in a channel flow. The original AKN model (using linear eddy viscosity) is also included. The values in the y-axis are normalized by u_τ.

$$\overline{u_j t} = -C_t \tau \left(\overline{u_j u_k} \frac{\partial T}{\partial x_k} \right), \tag{17}$$

where $C_t = 0.3$. When the model is integrated to the wall, the turbulent time-scale τ should be treated carefully. One approach is to use a damping function (see, Rokni 1998); however, another approach is to bound τ based on more physical grounds. Durbin (1993), for example, used the fact that the physical time-scale cannot be smaller than Kolmogorov time-scale, so that

$$\tau_{\min} = 6\sqrt{\frac{\nu}{\varepsilon}}. \tag{18}$$

This form prevents $1/\tau$ from becoming infinite near the wall. Behnia et al. (1998), following the analysis of Durbin (1996) based on realizability constraints, used an expression of the form:

$$\tau_{\max} = \frac{C_R}{\sqrt{6} C_\mu |\eta|} \tag{19}$$

for an upper bound on the turbulent time-scale. The value of C_R chosen here is 0.46 which is consistent with the value used by Behnia et al. (1998). (Note that Behnia et al. used the normal fluctuating velocity $\sqrt{\overline{v^2}}$ as the characteristic velocity scale; whereas here $\sqrt{k}$ is used.) Nevertheless, it was found that the temperature profile was relatively insensitive to the exact value of C_R chosen.

3. Boundary condition and numerical solution procedure

For the fully developed duct flows under investigation, periodic conditions can be imposed in the streamwise direction. This significantly reduces the computational cost since the number of grid points in the streamwise direction can be minimized. For the wavy duct case, the domain under investigation is assumed to be a subset of a larger field, which is composed of a periodic (streamwise) array of such (wavy) bends. In this case, periodic streamwise boundary conditions are applicable as well.

The pressure P decreases in the streamwise direction, so this variable needs to be handled in a special way if periodic conditions are to be imposed. It is first assumed that the pressure field can be expressed as:

$$P(x,y,z) = -\beta x + P^*(x,y,z), \tag{20}$$

where β is a constant representing the non-periodic pressure gradient and P^* behaves in a periodic manner from cycle to cycle in the streamwise direction.

The temperature field increases (or decreases) depending on the wall surface temperature, and is not periodic in the fully developed region. However, the scaled (dimensionless) temperature, given by $\theta(x,y,z) = (T(x,y,z) - T_{\text{wall}})/(T_{\text{bulk}} - T_{\text{wall}})$ is periodic. When the scaled variable $\theta(x,y,z)$ is inserted into Eq. (3), a scaled energy equation is obtained with additional source terms. More details can be found in Rokni (1998). Temperature field results presented throughout the remainder of the paper will be in terms of dimensionless variable $\theta(x,y,z)$.

When integrating directly to the wall, the wall conditions for k and ε are needed. Thus, $k = 0$ at the wall and the dissipation rate is set along the points adjacent to a wall as

$$\varepsilon = \nu \left(\frac{\partial \sqrt{k}}{\partial d_w} \right)^2 \approx 2\nu \frac{k}{d_w^2}, \tag{21}$$

where d_w is the normal distance from the wall to the point adjacent to the wall.

The numerical method is based on the finite volume technique, with a non-staggered grid arrangement, by transforming from the physical space (Cartesian system) into the computational space (general coordinate system). The Rhie–Chow interpolation method is employed to interpolate the velocity components to the control volume faces from the grid points. The SIMPLEC algorithm is used for the pressure–velocity coupling. A modified SIP method is implemented for solving the equations. The QUICK scheme is used for treating the convective terms in the momentum equations; however, in order to achieve stability in the k and ε equations, a hybrid scheme is used for the convective terms. The computations were terminated when the sum of the absolute residuals normalized by the inflow was less than 10^{-6} for all variables. A further discussion of the specification and implementation of the boundary conditions, as well as the numerical procedure used in the solution of the mean and turbulent equations, can be found in Rokni (1998).

4. Results

A major focus of this study is to analyze the effect of introducing streamwise waviness into duct geometries with fully developed, three-dimensional flow. The cross-sections under investigation are rectangular, trapezoidal, and triangular since each of these has been individually studied previously in either straight and/or wavy duct geometries. The study here parameterizes the problem so the aspect ratio of all three cross-sections is the same. Only one-half of the duct geometry within the cross-sections needs to be considered due to the symmetries of the flows in the y–z plane. A sketch of one of the duct configuration (trapezoidal cross-section) is shown in Fig. 2. The other cross-sections under investigation (rectangular and triangular) are simply obtained by changing the base-angle, and as noted, the cross-section aspect ratio for all the cases is 5 to 3.

Results for mean velocity, mean temperature, friction factor and Nusselt number are presented. Emphasis is placed on the secondary flow patterns generated as well as the temperature and velocity contours within the ducts. A comparison of the secondary flow fields, streamwise velocity and temperature, between the straight and wavy duct configurations are pre-

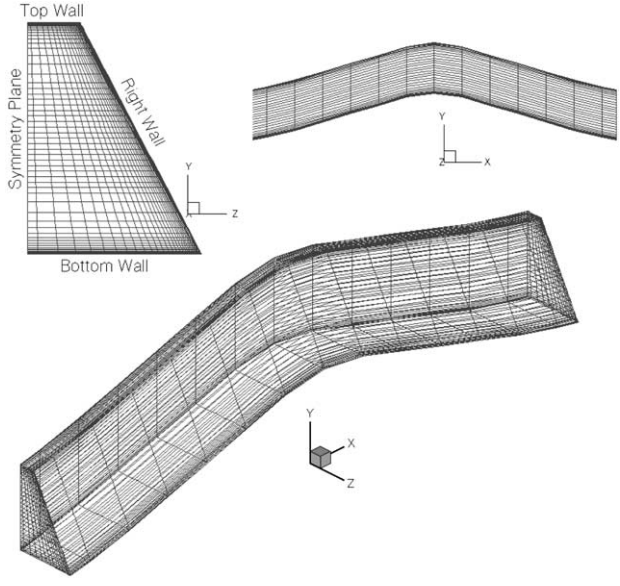

Fig. 2. Sketch of trapezoidal duct configuration.

sented in order to assess the effect of waviness on the flow dynamics.

A grid independence study was undertaken at the outset. Both grid placement (stretching) and number of grid points were assessed. Quantities such as friction factor and Nusselt number were compared to analytic correlations, and velocity and temperature contours were compared on different grids for each geometry. Thus, the results presented are based on sufficiently resolved computational flow fields.

4.1. Straight rectangular duct

In Fig. 3, the secondary flow velocity vectors in the fully developed rectangular duct are shown at a Reynolds number of 1.1845×10^4. The predictions are in good agreement with experimental observations. Such secondary flow patterns were first observed by Nikuradse during his experiments with non-circular ducts (see, Kakaç et al., 1987). As is well known, in laminar flow these secondary motions do not occur. The calculated friction factor and *Nu*-number are 7.383×10^{-3} and 36.2, respectively, and the calculated center-to-bulk-velocity ratio (U_c/U_b) is 1.23. These values for the friction factor and *Nu*-number are in excellent agreement with the Prandtl friction law and Dittus–Boelter correlations, which yield 7.387×10^{-3} and 37.8, respectively. In this study, the Prandtl friction law (Incropera and DeWitt, 1996) is given by

$$\frac{1}{\sqrt{4f_{Pr}}} = 2\log\left(Re\sqrt{4f_{Pr}}\right) - 0.8 \tag{22}$$

and the calculated Dittus–Boelter correlation (Incropera and DeWitt, 1996) for *Nu*-number is given by

$$Nu_{DB} = 0.023Re^{0.8}Pr^{0.3}, \tag{23}$$

where the *Re*-number is based on the hydraulic diameter defined as

$$D_h = \frac{4A_{cross}}{a + b + \frac{h}{\sin\varphi}} \tag{24}$$

with a, b, h and φ the base length, upper length, height and base angle, respectively. A_{cross} is the cross-section area which can be defined as $0.5h(a+b)$ for all the cases considered here.

In turbulent flow, the forces driving the secondary motion are concentrated in the region close to each corner. These motions are generated by gradients of the normal turbulent stresses. However, the linear eddy viscosity model (see e.g., Rokni and Sundén, 1998) does not correctly predict these secondary motions because of its inability to accurately account for the individual normal Reynolds stresses $\overline{u_i u_i}$ (no sum). Since the flow is fully developed, the $\overline{uu}$ normal stress is simply $2k/3$. Speziale (1982) has shown that secondary flow will develop only if the streamwise mean velocity gives rise to any non-zero normal Reynolds stress difference in planes perpendicular to the mean flow direction. For linear eddy viscosity models, this is not the case so there is no V or W mean velocity generated and as such $\overline{vv}$ and $\overline{ww}$ are equal to $2k/3$.

4.2. Straight trapezoidal duct

The velocity vectors, the corresponding mean flow and mean temperature contours predicted by the EASM in a trapezoidal duct (with the same aspect ratio as in the rectangular duct) are presented in Fig. 4 for a *Re*-number of 1.1841×10^4. As shown in the figure, there exist two counter-rotating vortices close to each corner (cf. Rokni and Sundén, 1996). The calculation required 61×31 grid points in the cross-section (the same as was used for the rectangular duct). The calculated friction factor and Nu-number are 7.591×10^{-3} and 37.5, respectively, and the center-to-bulk-velocity ratio (U_c/U_b) is calculated as 1.25. These values for the friction factor and *Nu*-number compare favorably with the Prandtl friction law and Dittus–Boelter correlations (Eqs. (22) and (23)), which yield 7.387×10^{-3} and 37.8, respectively.

Close to the top side corner (top wall and right wall junction) two counter-rotating vortices are generated – a small one and a much larger one – which are divided along the corner-bisector. The smaller vortex size decreases with decreasing top wall length until it vanishes for a triangular duct. Correspondingly, the large vortex size increases while this length decreases. This same secondary flow pattern was also observed in a triangular duct in the experiment of Nikuradse (see e.g. Kakaç et al., 1987).

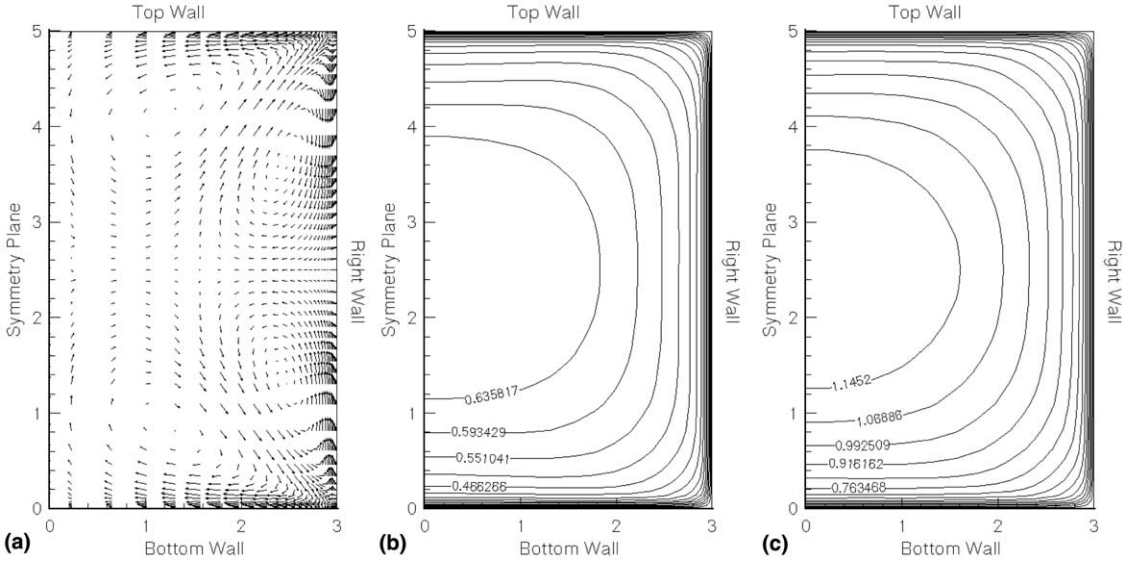

Fig. 3. Predicted secondary motion velocity vectors (a), mean streamwise velocity contours (b) and mean dimensionless temperature (c) in a rectangular duct.

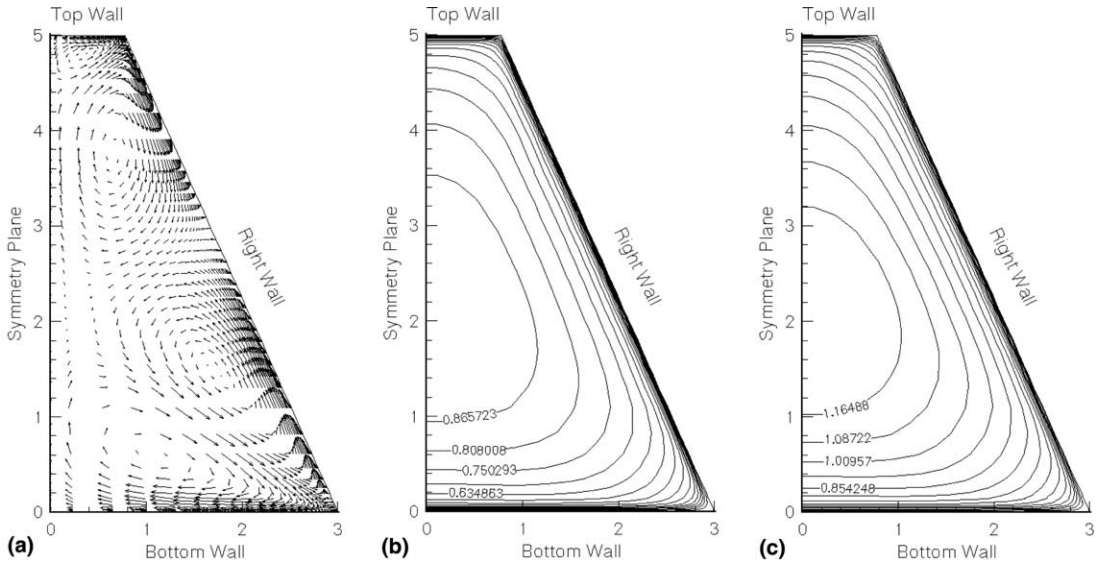

Fig. 4. Predicted secondary motion velocity vectors (a), mean streamwise velocity contours (b) and mean dimensionless temperature (c) in a trapezoidal duct.

Close to the bottom side corner (bottom wall and right wall junction) two counter-rotating vortices are generated and are divided along the corner-bisector. The vortex below the bisector induces flow along the bottom wall towards the center of the duct; whereas, the vortex above the bisector induces flow upward along the right wall. As the figure shows, at some point along the right wall, the wall shear stress ($= v\partial V_s/\partial n$, where V_s is the tangential velocity in the y–z plane and n is the direction normal to the surface) is zero.

Results from the calculations of secondary motions in trapezoidal ducts have been reported previously by Rokni and Sundén (1996); however, wall functions were used which precluded application at such low *Re*-numbers. It was also found that the methodology used there was limited to trapezoidal ducts with small height-to-base ratio and was not able to predict the secondary motions down the walls as accurate as the present model. Rokni (2000) predicted similar secondary motions by introducing damping functions into the tensor representation of the Reynolds stress. This is in contrast to the present study where no damping functions (for the Reynolds stresses) are used.

4.3. Straight triangular duct

The calculation procedure used here makes it possible to apply the present model to triangular ducts and to predict turbulence quantities without any convergence problems. In the geometry shown in Fig. 5, the top wall length is much smaller than the other two sides ($\approx 3 \times 10^{-3}$ of the duct height). This length cannot be set to zero since using structured grids in the calculations requires that no side of any control volume in the domain be zero. Nevertheless, this very small top wall

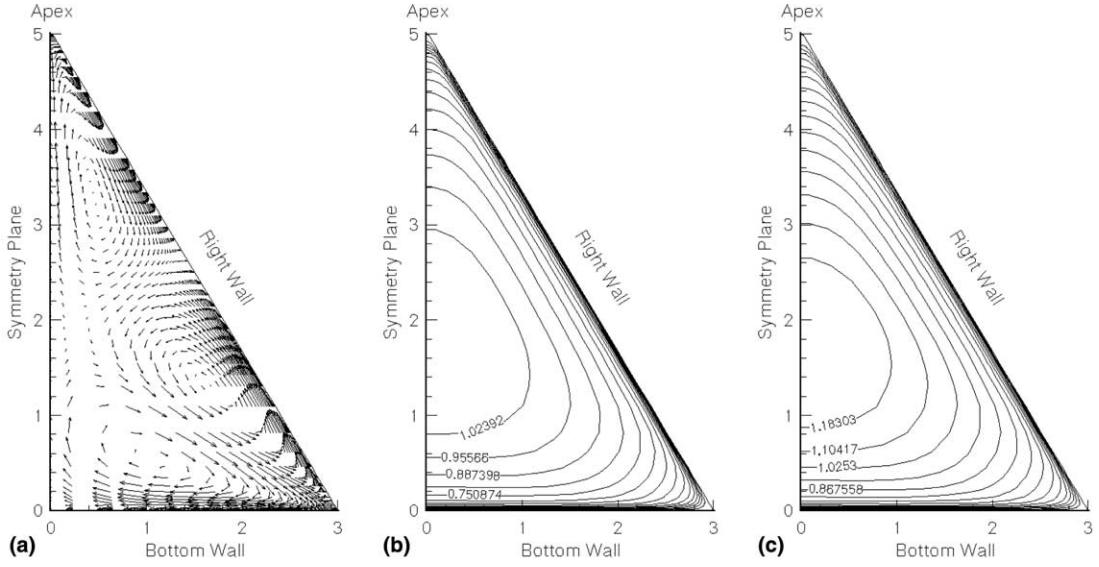

Fig. 5. Predicted secondary motion velocity vectors (a), mean streamwise velocity contours (b) and mean dimensionless temperature (c) in a triangular duct.

length is assumed to yield the correct limiting behavior of a sharp corner. These kinds of geometries are difficult to compute with higher-order turbulence closure models because of the large gradients occurring in relatively small spatial regions. Second-moment closures, for example, would be especially susceptible to numerical stiffness problems. Such constraints reveal the usefulness of algebraic stress models. On the one hand, a non-linear eddy viscosity model is needed to calculate the correct secondary flow behavior, while on the other hand, a closure model needs to be used which can also be integrated to the wall (robustly) in order to capture the key dynamics.

The predicted cross-velocity and temperature fields for the triangular duct at a *Re*-number of 1.1557×10^4 are shown in Fig. 5. The predicted Fanning friction factor and *Nu*-number (GGDH model) are 7.591×10^{-3} and 36.2, respectively which compare favorably with the Prandtl friction law and Dittus–Boelter correlation, Eqs. (22) and (23), values of 7.434×10^{-3} and 37.1, respectively. The center-to-bulk-velocity ratio (U_c/U_b) is calculated as 1.27. Consistent with the forced convection problem under study, the temperature contours shown in Fig. 5(c) display the same qualitative behavior as the velocity contours (Fig. 5(b)).

The aspect ratio as well as the number grid used in the cross-section is the same as in the previous ducts.

4.4. Wavy ducts

In order to analyze the effect of waviness in the duct on the flow field dynamics, the same three cross-sections used in the straight duct calculations are now introduced into a wavy duct geometry. In a previous study, Rokni and Sundén (1998) analyzed the flow in a wavy duct using the non-linear eddy viscosity model of Speziale (1987). In that study, the waviness was confined to the *x–z* plane. In order to retain the symmetry of the duct cross-sections in the *y–z* plane, the waviness in the duct here is confined to the *x–y* plane (see Fig. 2). The cross-section of the ducts has an aspect ratio of 5 to 3 – which is the same as the straight section ducts shown in Figs. 3–5. The ducts are assumed to be "infinitely" long in the streamwise (x) direction, several "wavelengths" away from the duct inflow, the flow in each successive section (equal to one-wavelength of the cyclic variation should be the same (i.e., fully developed)). With the sinuous variation in the *x–y* plane, the flow retains its symmetry in the *y–z* plane, and with the flow assumed to be fully developed, it is consistent to apply periodic (cyclic) conditions at boundaries that are a wavelength apart. The length chosen for the ducts in the computational domain is 7.5 times the height and the maximum deflection is one duct-height. The number of grid points in the cross-section is 61×31 for the *y*- and *z*-directions, respectively, which is the same for the straight section ducts. The Reynolds number for the wavy duct with rectangular cross-section is 1.2216×10^4, which is slightly higher than the corresponding straight duct case. The Reynolds number for the wavy trapezoidal duct is 1.1913×10^4, and for the wavy triangular duct is 1.1555×10^4, which are very close to the corresponding straight ducts. Due to computer limitations, 40 grid points, uniformly spaced, are set in the streamwise, or *x*-direction and, for convergence, the residuals reached 10^{-3} for the temperature equation and 10^{-4} for both the velocity equations and 10^{-4} for the turbulence equations.

The wavy duct geometry suggests a complicated vortical flow field within the duct where components of vorticity in the cross-stream and streamwise directions may simultaneously exist. In order to see how the waviness influences the flow in the duct, the secondary motion velocity vectors and streamwise velocity contours are shown at two different cross-sections in Figs. 6–8. Fig. 6 shows the secondary velocity vectors at the inlet and Fig. 7 shows the secondary motions at the bend cross-sections of the wavy ducts. These secondary motions can be compared with the secondary motions of the corresponding straight duct with the same cross-section shown in Figs. 3–5, respectively.

Neither the velocity vectors at the inlet nor the bend show the same coherence and structure as the velocity vectors in the straight duct. This, of course, implies that the flow structure throughout the wavy duct has been altered as well. In addition, the magnitude of the secondary flow is approximately 10 times larger than the secondary flow in the straight duct with similar cross-section (i.e., 20% of the streamwise flow). At the inlet plane, the flow is more confined to the wall region where the flow is along the right wall moving from the bottom to the top. While in the straight duct four (three) distinct vortical structures could be clearly seen, the inlet of the wavy duct has only two dominating structures – each biased towards the right wall.

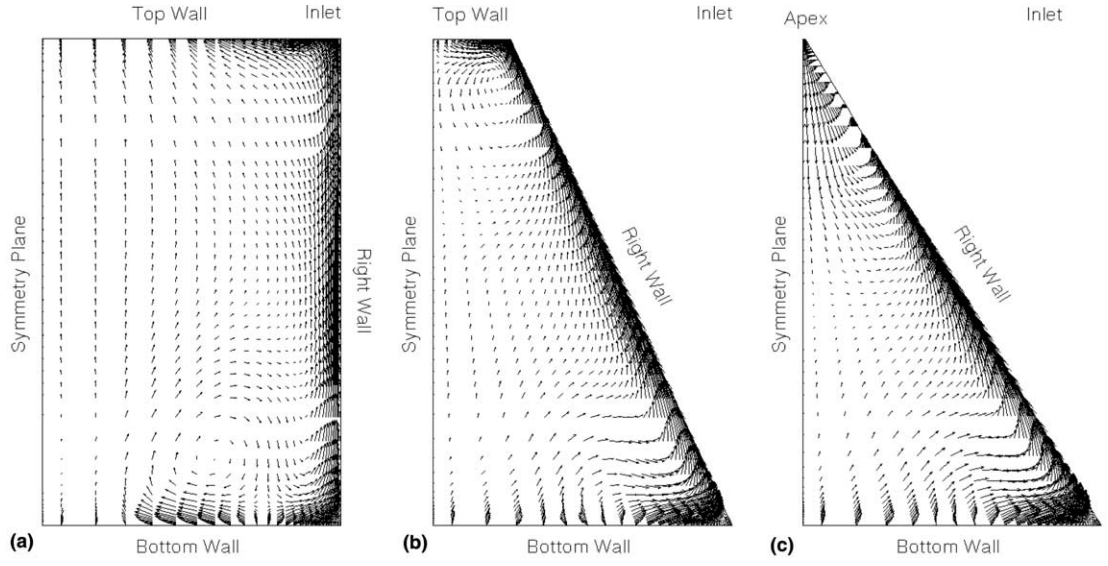

Fig. 6. Secondary motion velocity vectors at the inlet cross-sections of the wavy ducts: (a) rectangular, (b) trapezoidal, (c) triangular ducts.

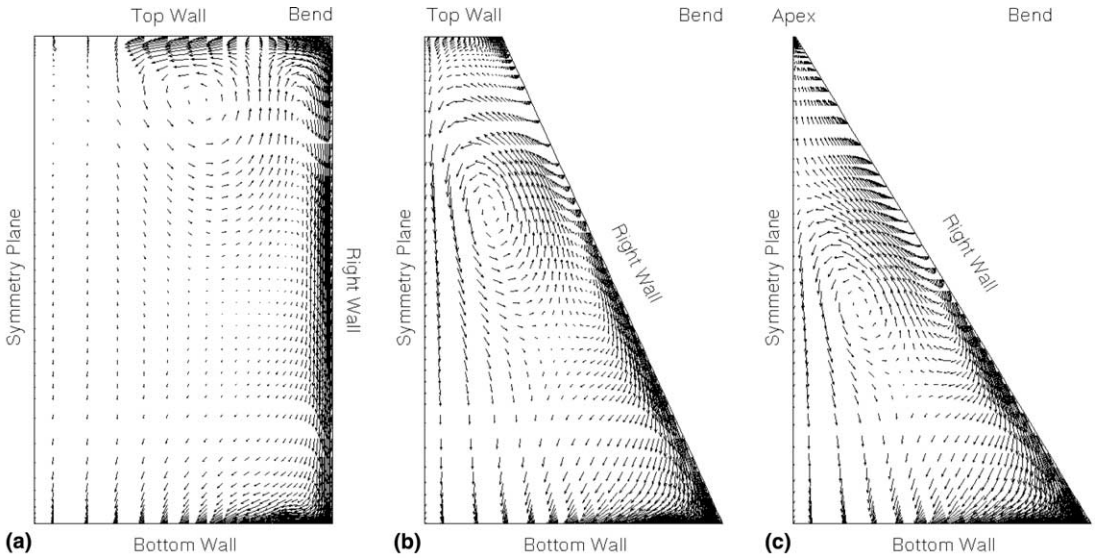

Fig. 7. Secondary motion velocity vectors at the bend cross-sections of the wavy ducts: (a) rectangular, (b) trapezoidal, (c) triangular ducts.

Clearly the streamwise duct curvature has a significant impact on the flow in the cross-section. Since the cross-section secondary motion is a consequence of the turbulent normal stress difference, the change in cross-section flow pattern from the straight duct must be due to the change in the turbulence in the flow field. As seen from Fig. 2, the inlet cross-section is located at a trough in the "infinitely" long duct. As such, upstream of the inlet (or outlet owing to the cyclic geometry) of the computational domain, the flow in the bottom of the duct is bounded by a surface with predominant convex curvature. Since a convex curved surface suppresses the turbulence activity in its' vicinity relative to a flat surface, the vortical structure which appeared adjacent to the bottom wall below the corner-bisector in the straight duct (cf. Fig. 3(a), 4(a) and 5(a)) is significantly weakened, and the vortical structure which lies above the corner-bisector now dominates the flow in the lower part of the duct. For the rectangular duct the vortical structure that lies below the bottom corner-bisector is strongest compared to the corresponding vortices in the other two ducts, while the same vortex in the triangular wavy duct is weakest. This can be explained due to the geometrical structure and turbulent stresses in the cross-flow. An opposite situation occurs in the top half of the duct where the surface curvature is predominantly concave upstream of the inlet (or outlet) of the computational domain. The vortical structure, which appeared adjacent to the top wall, and above the corner-bisector (top wall and right wall junction), has now intensified, and the larger vortical structure that appeared below the corner-bisector has weakened significantly for both rectangular and trapezoidal wavy ducts. However, since in the straight triangular duct there was not any vortical structure adjacent to the top wall, as in the rectangular and trapezoidal duct (vortical structure above the bisector) to be intensified, then the corresponding vortical structure is so weakened that it has vanished. Thus, the appearance of the counter-clockwise rotation at the apex can be explained due to the displacement of the vortical structure from the bottom wall above the corner-bisector. This means that the vortical structure that lies above the corner-bisector of the bottom wall in the triangular wavy duct is so intensified that it now extends to near the apex.

It should be noted that the waviness itself can induce some secondary motions in the duct as well due to the non-zero vertical velocity along the duct. In recent studies by Rokni and Sundén (1998) and Asako et al. (1998), similar wavy duct geometries were studied with a turbulent flow (Rokni and Sundén) and a laminar flow (Asako et al. (1998)). It was found that the geometry driven secondary flows (laminar case) were much smaller than the turbulence driven secondary flows and could be neglected. In addition, the laminar flow secondary motions were found to be different in detail from the turbulence driven secondary motions.

An analogous scenario can be described at the bend with the vortical flow along the bottom wall being intensified, and the vortical flow along the top weakened (Fig. 7). In fact, the counter-clockwise rotation of the velocity vectors in the upper half of the duct suggest that this vortex may have been displaced upward from the lower half of the channel and corresponds to the vortical structure which appeared above the lower wall corner-bisector in the straight duct. Another clockwise rotation which appears close to the right wall suggests that this vortex has been displaced downward from the top wall (or apex) and corresponds to the vortical structure which appeared below the corner-bisector (or near the apex) in the corresponding straight duct. This vortex has been significantly weakened compared to the corresponding straight duct. The size of this vortex is much larger than the ones in the trapezoidal and triangular ducts due to angle of the corner. Another interesting point is that in the triangular wavy duct there exists a recirculation zone downstream along the apex (cf. Fig. 12(a)). The vectors toward the apex correspond to this recirculation zone.

Fig. 8 shows the streamwise velocity contours at both the inlet and bend. As expected, the velocity magnitudes across the duct remain relatively the same, the region of maximum velocity moves from the upper half of the cross-section at the inlet to the lower half of the cross-section at the bend. These locations are in (qualitative) contrast to the velocity contours in the straight duct where the maximum velocity is relatively "centered" in the cross-section. It will be shown shortly (Table 1) that such a change in the streamwise velocity field has a significant effect on the friction factor of the wavy duct compared to the straight duct.

In forced convection problems, the temperature field has qualitative features that are characterized by the streamwise velocity field. In Fig. 9 are shown the mean temperature contours at the inlet and bend cross-sections. The distribution of

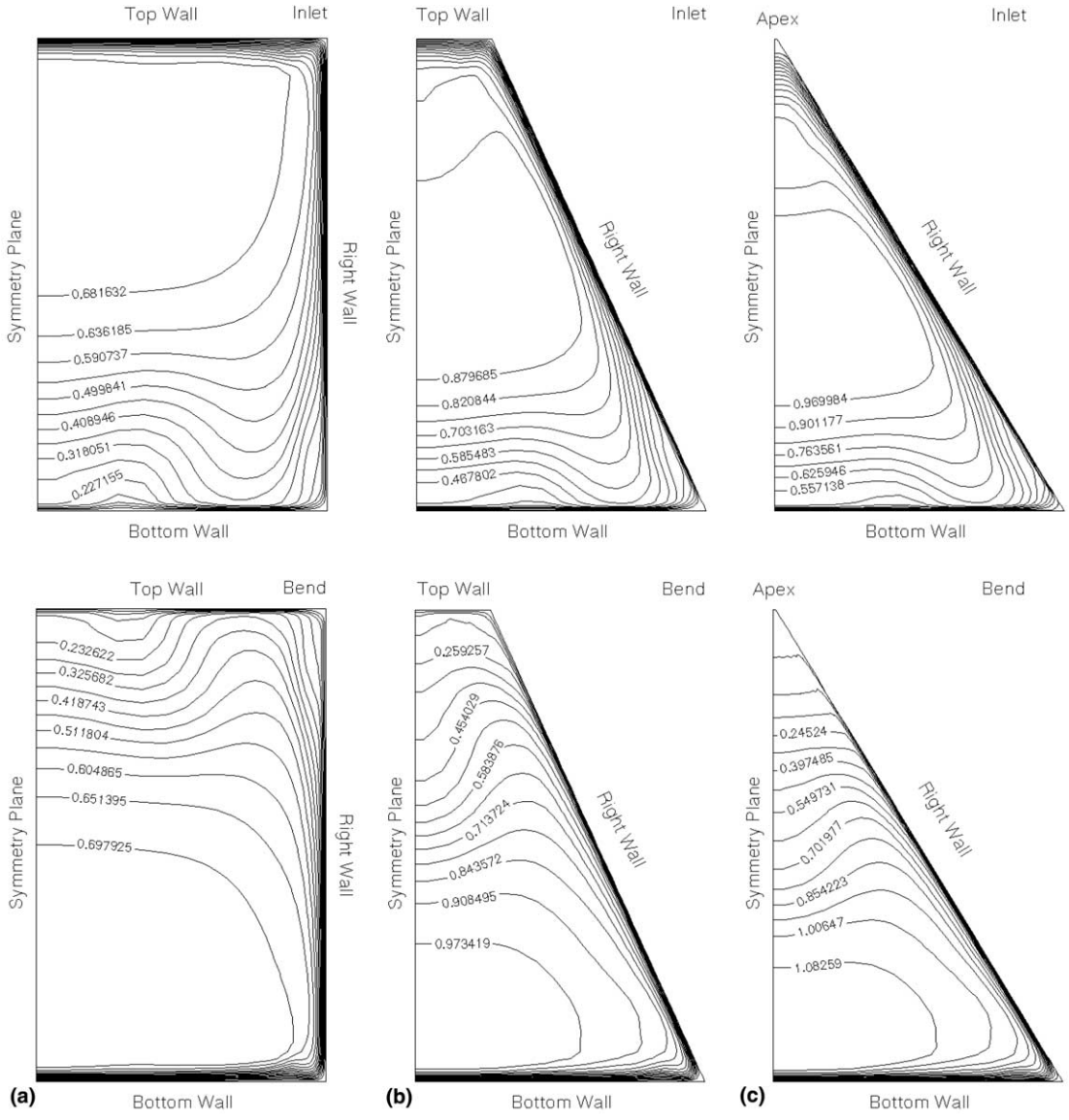

Fig. 8. Streamwise velocity contours at two different cross-sections of the wavy ducts: (a) rectangular, (b) trapezoidal, (c) triangular ducts.

temperature contours suggests a significant increase in overall heat transfer compared to the straight duct (see Table 1). Consistent with the velocity contours at the inlet (Fig. 8, inlets) there is a rapid rise in the temperature distribution near the bottom corner-bisector (Fig. 9, inlets). This is due to the existence of the counter-clockwise rotating vortex that now dominates near the bottom wall in the wavy duct.

It should be pointed out that the scenario described here is limited to the 5 to 3 ratio duct, other aspect ratios could produce different flow patterns and subsequently different distributions of streamwise velocity and temperature. For example, if the height-to-length ratio were decreased to 3 to 3, the vortex adjacent to the top wall in a straight duct flow would be larger than in the 5 to 3 cross-section. In the corresponding wavy duct (with the same cross-section) this vortex would most likely survive and contribute to the cross-section dynamics. Obviously, the choice of optimal configuration is a rather exhaustive process and certainly outside the scope of the current study.

Table 1
Comparison between wavy duct and straight duct friction factor and Nusselt number for similar cross-sections

Wavy duct cross-section	f/f_{Pr}	Nu/Nu_{DB}
Rectangular	1.86	1.26
Trapezoidal	1.78	1.26
Triangular	1.73	1.26

The streamwise velocity and temperature contours in the x–y plane at two different z-locations are shown in Fig. 10–12, for rectangular, trapezoidal and triangular wavy ducts, respectively. The figures show that a strong recirculation zone exists along the top wall of the triangular wavy duct downstream of the inlet to the computational domain (Fig. 12(a)). Such strong recirculation zone exists in any plane along the apex. For the trapezoidal wavy duct, in the symmetry plane a small recirculation zone exists along the top wall downstream of the inlet to the computational domain, which gradually weaken in the other plane and almost vanishes in the middle plane. The recirculation zone is much weaker for the trapezoidal wavy duct and almost vanishes in the rectangular wavy

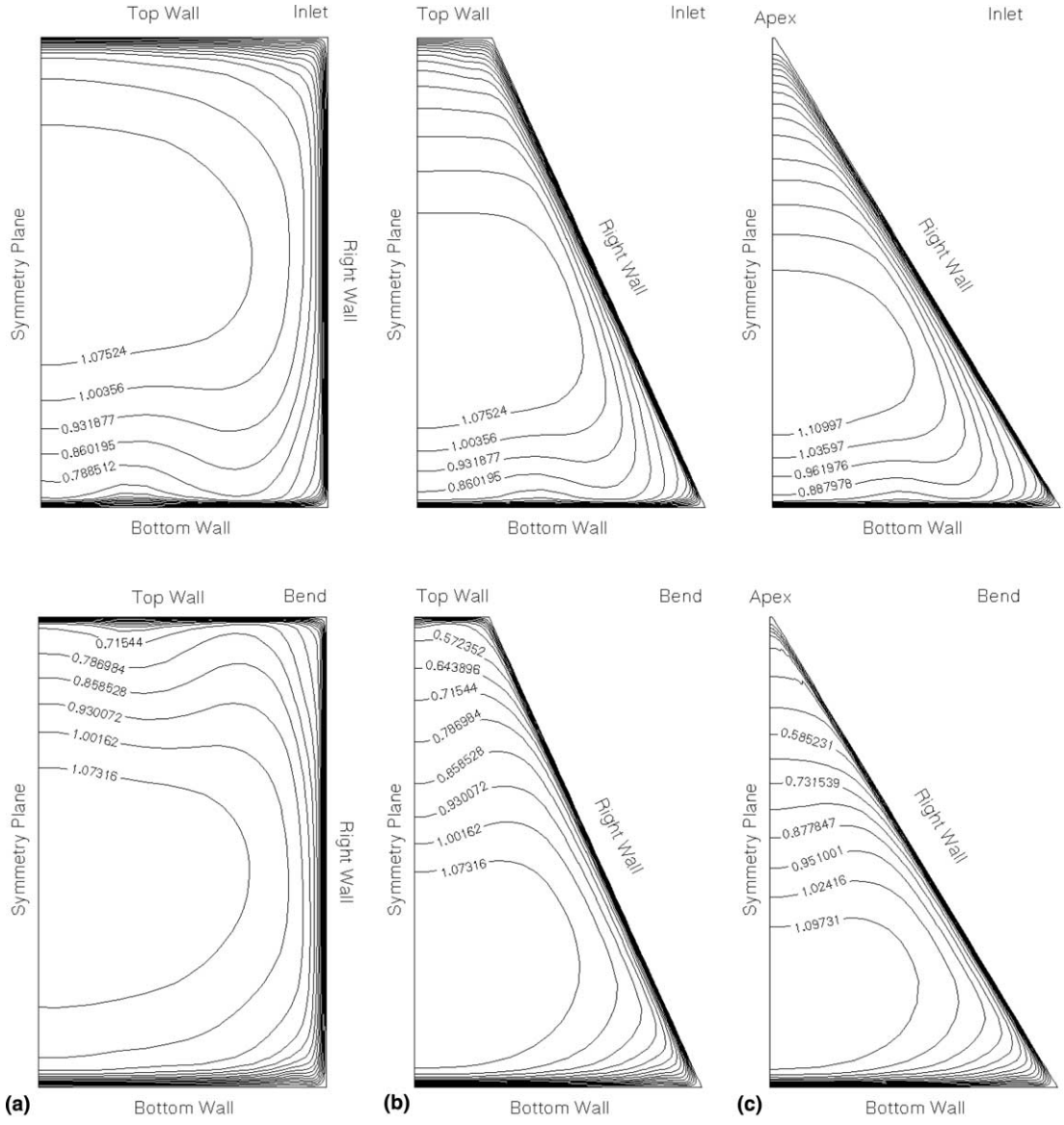

Fig. 9. Dimensionless temperature contours at two different cross-sections of the wavy ducts: (a) rectangular, (b) trapezoidal, (c) triangular ducts.

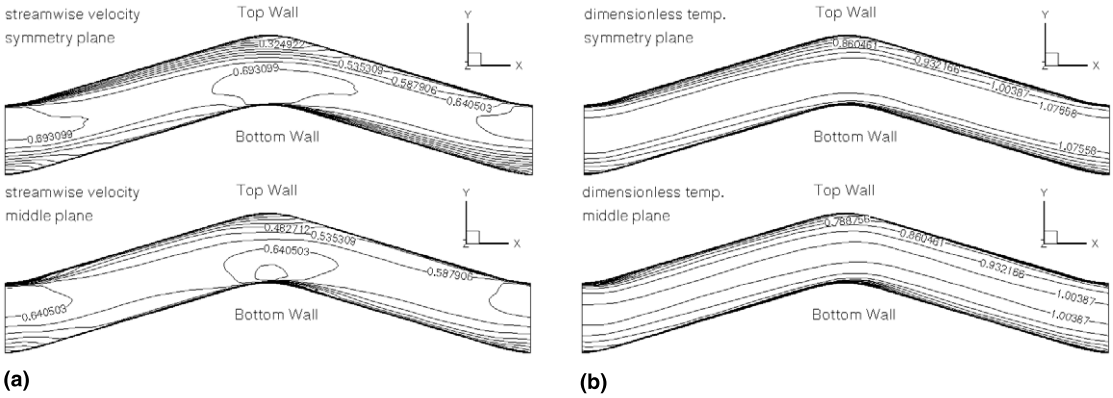

Fig. 10. Streamwise velocity contours and dimensionless temperature contours at symmetry plane and middle plane of the rectangular wavy duct: (a) velocity, (b) temperature.

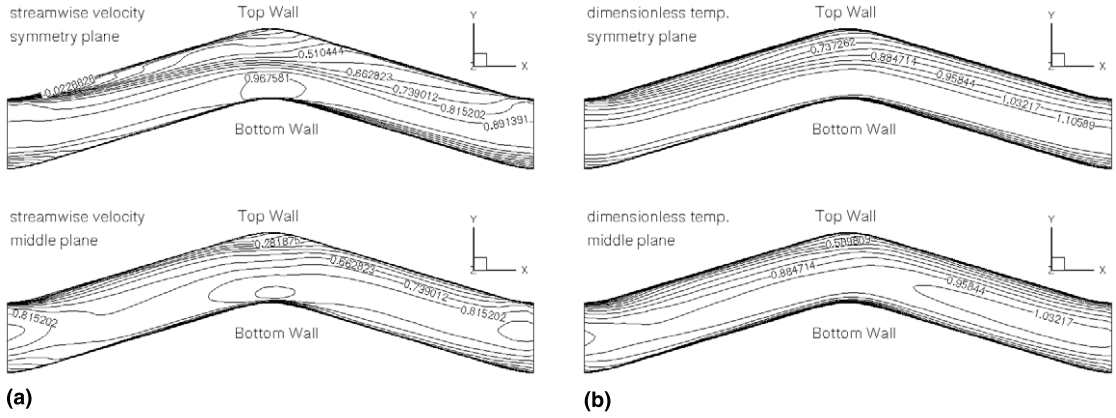

Fig. 11. Streamwise velocity contours and dimensionless temperature contours at symmetry plane and middle plane of the trapezoidal wavy duct: (a) velocity, (b) temperature.

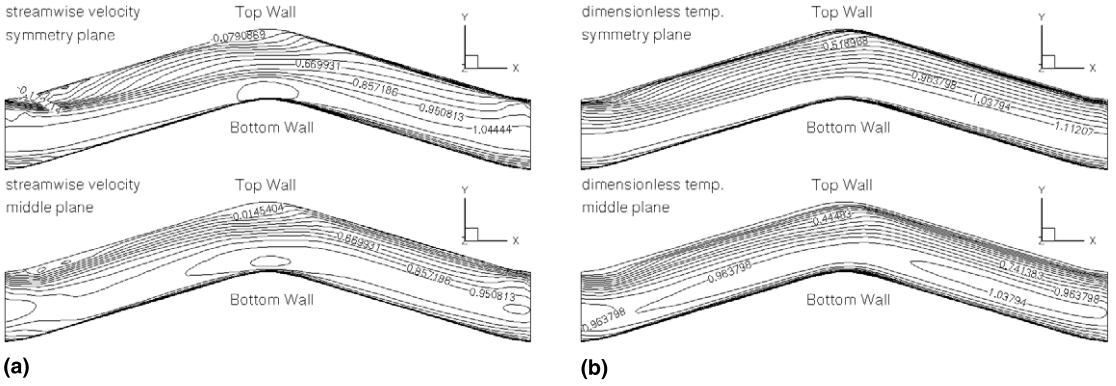

Fig. 12. Streamwise velocity contours and dimensionless temperature contours at symmetry plane and middle plane of the triangular wavy duct: (a) velocity, (b) temperature.

duct. Such a re-circulation zone does not exist at all in the rectangular wavy duct, in any corresponding plane. Thus, coupled with the effect of different cross-section aspect ratios, the streamwise variation (radii of curvature of the bend and inlet regions) of the duct will also significantly affect the flow.

The streamwise variation of the temperature distribution is shown in Figs. 10(b), 11(b) and 12(b). The distribution at the symmetry plane is consistent with the results shown in Fig. 9. There, the region of peak temperature occurs in the upper half of the inlet plane and at the bend it occurs near the lower half of the cross-section. This is also shown in Figs. 10(b), 11(b) and 12(b) along with the more complex temperature distribution in the middle plane. In the middle plane, the maximum temperature within the domain is located in a region just downstream of the bend.

Table 1 shows the calculated friction factor and *Nu*-number for the wavy ducts. The friction factors in the table are normalized by Prandtl friction law, and the Nusselt numbers are normalized by Dittus–Boelter correlation. As noted previously in the discussion of the straight duct results, the friction law and Dittus–Boelter correlation provide an accurate measure of both the friction factor and *Nu*-number so that the normalization provides a measure of how the waviness affects these hydraulic parameters relative to the corresponding straight duct. As can be seen from Table 1, both the friction factor and the *Nu*-number for the wavy duct are much higher than the straight duct. While the idea of having a duct with waviness in the streamwise direction is to increase the heat transfer coefficient, the associated cost may be a dramatic increase in the friction factor as well. The table also shows that the heat transfer coefficient is increased by about 26%, while the friction factor is increased by about 80%, relative to the corresponding straight duct. The triangular wavy duct considered here has the best performance, since the increase in the friction factor is less than the other two wavy ducts, while it increases the heat transfer by the same factor as the trapezoidal and rectangular duct. The associated cost for the friction factor in the wavy rectangular duct is highest. In many industrial applications, it is necessary to reach an adequate balance between the desired increase in heat transfer and increased cost associated with an increase in friction factor.

However, other factors such as manufacturing costs may enter into the analysis for choosing the most efficient duct configuration. For example, while the trapezoidal duct has a higher friction factor ratio, it is only slightly larger than the triangular cross-section duct that may be costly to fabricate.

5. Summary

The results from the numerical solution of fully developed, three-dimensional turbulent duct flow under isothermal conditions have been presented for straight and wavy ducts with rectangular, trapezoidal, and triangular cross-sections. The turbulent stresses were modeled using an EASM, and the turbulent heat fluxes were modeled by a GGDH model. The

present EASM was solved with a low-Reynolds number version of the k–ε equations to predict the flow field for all the geometries with Reynolds number up to 10^5. A bounded (lower and upper) time-scale was introduced for the GGDH model. The calculation procedure was found to be robust, with limited demand on the total number of grid points. Comparisons with well-established correlations, extracted from experimental studies, showed excellent agreement for the hydraulic parameters (friction factor and *Nu*-number). Qualitative comparisons with observed secondary flow patterns were also found to be in excellent agreement. A detailed comparison between three wavy ducts and straight duct geometries with similar (rectangular, trapezoidal, and triangular) cross-sections was made. Several interesting contrasts in flow structure were highlighted which suggested the need for a more through and systematic study of such sinuous flows. For example, it was found that the cross-flows are much stronger than the corresponding ones in the straight ducts, a feature that can significantly decrease the fouling problems in heat exchangers.

The results also suggest that while the model for the heat flux can be relatively simple under isothermal conditions, this simplicity does not necessarily preclude an accurate prediction of either the velocity or temperature fields in geometries of practical industrial interest. However, higher-order turbulence models are required due to the necessity of accurately predicting the turbulent Reynolds stresses which, in turn, generate the mean secondary motions within each cross-section. While this requirement precludes the use of linear eddy viscosity models, the desire to calculate the flow in such complex geometries also precludes straightforward application of full differential second-moment closures. The (explicit) algebraic stress closure level of modeling is, therefore, well-suited for such computations. In addition, higher-order closures for the heat fluxes may also be required in non-adiabatic cases and/or in cases where counter-gradient heat transfer occurs. Correspondingly explicit algebraic heat flux models, coupled with equations for the temperature variance and variance dissipation rate, could be applied to such flows.

Acknowledgements

The first author would like to thank the Bengt Ingeströms Foundation (in Sweden) for financial support during the course of this study.

References

Abe, K., Kondoh, T., Nagano, Y., 1995. A new turbulence model for predicting fluid flow and heat transfer in separating and reattaching flows-II. Thermal field calculations. Int. J. Heat Mass Transfer 38 (8), 1467–1481.

Asako, Y., Faghri, M., Sundén, B., 1998. Three-dimensional laminar forced convection characteristics of wavy ducts with trapezoidal cross section for plate-fin heat exchanger. In: Sundén, Faghri (Eds.), Computer Simulations in Compact Heat Exchangers, vol. 1. Computational Mechanics Publications, Southampton (Chapter 3).

Behnia, M., Parneix, S., Durbin, P.A., 1998. Prediction of heat transfer in an axisymmetric turbulent jet impinging on a flat plate. Int. J. Heat Mass Transfer 41 (12), 1845–1855.

Durbin, P.A., 1993. A Reynolds stress model for near wall turbulence. J. Fluid Mech. 249, 465–498.

Durbin, P.A., 1996. On the k–ε stagnation point anomaly. Int. J. Heat Fluid Flow 17 (1), 89–90.

Gatski, T.B., Speziale, C.G., 1993. On explicit algebraic stress models for complex turbulent flows. J. Fluid Mech. 254, 59–78.

Gavrilakis, S., 1992. Numerical simulation of low-Reynolds-number turbulent flow through a straight square duct. J. Fluid Mech 244, 101–129.

Huser, A., Biringen, S., 1993. Direct numerical simulation of turbulent flow in a square duct. J. Fluid Mech. 257, 65–69.

Incropera, F.P., DeWitt, D.P., 1996. Fundamentals of Heat and Mass Transfer, fourth ed.. Wiley, New York.

Jongen, T., Gatski, T.B., 1999. A unified analysis of planar homogeneous turbulence using single-point closure equations. J. Fluid Mech. 399, 117–150.

Kakaç, S., Shah, R.K., Aung, W. (Ed.), 1987. Handbook of Single-Phase Convective Heat Transfer. Wiley, New York, pp. 4.73–4.83.

Kim, J., Moin, P., Moser, R., 1987. Turbulence statistics in fully developed channel flow at low Reynolds number. J. Fluid Mech. 177, 133–166.

Launder, B.E., 1988. On the computation of convective heat transfer in complex turbulent flows. ASME J. Heat Transfer 110, 1112–1128.

Madabhushi, R.K., Vanka, S.P., 1991. Large eddy simulation of turbulence-driven secondary flow in a square duct. Phys. Fluids A 3, 2734–2745.

Meyer, L., Rehme, K., 1994. Large-scale turbulence phenomena in compound rectangular channels. Exp. Thermal Fluid Sci. 8, 286–304.

Rokni, M., 1998. Numerical investigation of turbulent fluid flow and heat transfer in complex ducts. Doctoral Thesis, ISSN 1104-7747, Division of Heat Transfer, Lund Institute of Technology, Sweden.

Rokni, M., 2000. A new low-Reynolds version of an explicit algebraic stress model for turbulent convective heat transfer in ducts. Numer. Heat Transfer B 37 (3), 331–363.

Rokni, M., Sundén, B., 1996. A numerical investigation of turbulent forced convection in ducts with rectangular and trapezoidal cross-section area by using different turbulence models. Numer. Heat Transfer 30 (4), 321–346.

Rokni, M., Sundén, B., 1998. 3D Numerical investigation of turbulent forced convection in wavy ducts with trapezoidal cross section. Numer. Meth. Heat Fluid Flow 8 (1), 118–141.

Rumsey, C.L., Gatski, T.B., Morrison, J.H., 2000. Turbulence model predictions of strongly-curved flow in a U-duct. AIAA J. 38 (8), 1394–1402.

Speziale, C.G., 1982. On turbulent secondary flows in pipes of noncircular cross-section. Int. J. Eng. Sci. 20, 863–872.

Speziale, C.G., 1987. On non-linear K–l and K–ε models of turbulence. J. Fluid Mech. 178, 459–475.

Speziale, C.G., Sarkar, S., Gatski, T.B., 1991. Modeling the pressure-strain correlation of turbulence: an invariant dynamical systems approach. J. Fluid Mech. 227, 245–272.

Su, M.D., Friedrich, R., 1994. Investigation of fully developed turbulent flow in a straight duct with large Eddy simulation. J. Fluids Eng. 116, 677–684.